Acta Cryst A FOUNDATIONS ADVANCES
ISSN 2053-2733

Interpretation of angular symmetries in electron nanodiffraction patterns from thin amorphous specimens

Amelia C. Y. Liu,[a]* Gregory R. Lumpkin,[b] Timothy C. Petersen,[c] Joanne Etheridge[d] and Laure Bourgeois[d]

[a]Monash Centre for Electron Microscopy and School of Physics, Monash University, Clayton, Victoria, 3800, Australia, [b]Australian Nuclear Science and Technology Organization, Lucas Heights, New South Wales, 2234, Australia, [c]School of Physics and Astronomy, Monash University, Clayton, Victoria, 3800, Australia, and [d]Department of Materials Science and Engineering and Monash Centre for Electron Microscopy, Monash University, Clayton, Victoria, 3800, Australia. *Correspondence e-mail: amelia.liu@monash.edu

Received 18 March 2015
Accepted 20 June 2015

Edited by S. J. L. Billinge, Columbia University, USA

Keywords: amorphous materials; electron nanodiffraction; short-range order; scanning transmission electon microscopy; Friedel symmetry.

The interpretation of angular symmetries in electron nanodiffraction patterns from thin amorphous specimens is examined. It is found that in general there are odd symmetries in experimental electron nanodiffraction patterns. Using simulation, it is demonstrated that this effect can be attributed to dynamical scattering, rather than other divergences from the ideal experimental conditions such as probe-forming lens aberrations and camera noise. The departure of opposing diffracted intensities from Friedel's law in the phase grating formalism is calculated using a general structure factor for disordered materials. On the basis of this, a simple correction procedure is suggested to recover the kinematical angular symmetries, and thus readily interpretable information that reflects the symmetries of the original projected object. This correction is numerically tested using both the phase object and multislice calculations, and is demonstrated to fully recover all the kinematical diffracted symmetries from a simulated atomic model of a metallic glass.

1. Introduction

Despite the lack of long-range order in amorphous materials and glasses it is thought that significant localized atomic ordering exists (Treacy *et al.*, 2005). This ordering can exist at several different length scales. At the length scale of nearest neighbours, the short-range atomic order (SRO) can be quite tightly dictated by efficient atomic packing in the case of metallic glasses, or covalent bonding in the case of amorphous semiconductors and network glasses. Order extended beyond this into the realm of medium-range atomic order (MRO) (1–3 nm) depends on how the local structural units may be packed or connected together (Treacy *et al.*, 2005). Broad beam diffraction experiments measure the average diffracted intensity that may be inverted by Fourier transform to yield the volume-averaged two-body atomic correlations. In amorphous and glassy materials the two-body correlations are not sufficient to distinguish between competing structural models and thus do not permit deep insight into the influence of structure on properties and behaviours (Treacy & Borisenko, 2012; Ziman, 1979).

Small volume diffraction measurements of complex disordered materials have a distinct advantage over broad beam measurements. In diffracted information from small volumes small fluctuations in atomic correlations due to local order are not averaged out. Two approaches have been developed to access the higher-order atomic correlation functions, based on

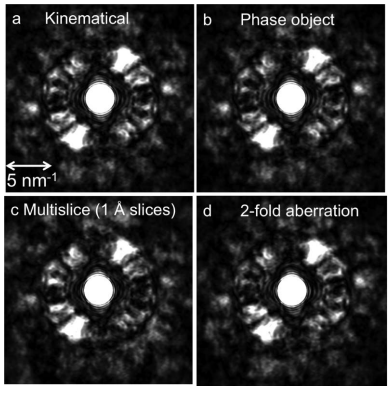

measuring diffracted information from volumes with size comparable to the SRO–MRO. The first, fluctuation electron microscopy, collects diffracted intensity from volumes with a size that encompasses the MRO of the material. By calculating the variance in this diffracted intensity from volume to volume, information that probes the four-body correlation function can be obtained (Treacy *et al.*, 2005). Unlike the average diffracted intensity, the variance cannot be inverted to obtain directly the correlation function. However, the data can be used to constrain atomic models using reverse Monte Carlo (Treacy & Borisenko, 2012). Angular correlations in electron nanodiffraction (END) patterns (Zuo & Tao, 2011; Cowley, 2002) have been used to access the local three-body correlation function or bond-orientational order in the short-range clusters of the material (Gibson *et al.*, 2010; Liu *et al.*, 2013; Howie *et al.*, 1985). For a thin, dense material in which the inter-nearest-neighbour cluster distance is comparable to the intra-nearest-neighbour cluster size, it has been shown by simulation both in the X-ray microdiffraction (Altarelli *et al.*, 2010; Kurta *et al.*, 2012) and electron nanodiffraction (Liu *et al.*, 2013) cases, that sensitivity to the orientational order within clusters is optimized by tuning the coherence length (X-rays) or size (electrons) of the probe to the size of the clusters. Even in this ideal condition, the angular cross-auto-correlation function (Wochner *et al.*, 2009) needs to be evaluated to quantify subtle angular correlations in the diffraction pattern from a column of disordered material containing several nearest-neighbour clusters (Liu *et al.*, 2013).

In the case of X-ray microdiffraction of colloids and electron nanodiffraction of metallic glasses, significant departures from Friedel's law were noted, that is, in general $I(\mathbf{k}) \neq I(-\mathbf{k})$ (Wochner *et al.*, 2009; Liu *et al.*, 2013). An extensive analysis of this behaviour and ramifications for the interpretations of such patterns was not undertaken. For X-ray microdiffraction, the breakdown was attributed to Ewald sphere curvature (Wochner *et al.*, 2009). For thin foils and energetic electrons the Ewald sphere may be well approximated as flat. For thin amorphous specimens, and a qualitative interpretation of diffracted intensities and phase-contrast images, the kinematical or weak-phase object approximation is sufficient to model the electron–specimen interaction (Cowley *et al.*, 1988). It has been observed that significant lens aberrations in the probe-forming lens will always result in a breakdown of Friedel symmetry in electron microdiffraction patterns of amorphous materials (Hÿtch & Chevalier, 1995; Rodenburg, 1988). An aberrated incident beam will add an imaginary component to the transmitted beam that will result in a breakdown of Friedel's law even if the kinematical approximation is employed for the electron–specimen interaction (Hÿtch & Chevalier, 1995).

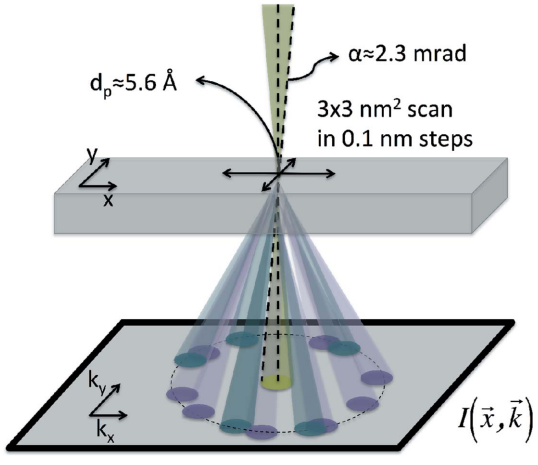

Figure 1
Schematic of SEND experiment.

In this contribution we examine angular symmetries in END from amorphous materials using optical parameters typical in an aberration-corrected scanning/transmission electron microscope (S/TEM). In this context, lens aberrations are no longer the major cause of the absence of exact π azimuthal rotational symmetry of nanodiffraction patterns. Rather, the asymmetry is due to dynamical diffraction in the diffracting volume. This multiple scattering complicates the interpretation of individual END patterns from disordered materials in terms of the symmetries of the original object. We analyse the asymmetry in END from amorphous objects in the phase grating (Cowley & Moodie, 1959) and dynamical (Cowley & Moodie, 1957; Fujimoto, 1959) formulations of electron diffraction. On the basis of our analysis we suggest a simple approach that can be applied to the average symmetries from an ensemble of nano-electron diffraction patterns to recover the average kinematical symmetries of the projected structure. In disordered specimens in which the number of coordination clusters in the diffracting column is limited, this approach may permit a quantitative measurement of symmetries of the nearest-neighbour clusters in the material.

2. Methods

A schematic of the scanning electron nanodiffraction (SEND) experiment in the S/TEM is shown in Fig. 1. An intense, quasi-parallel electron probe is scanned in 1 Å steps across a thin specimen. The full-field electron nanodiffraction pattern, $I(k_x, k_y)$, is collected at each point in the scanned array, (x, y). If dynamical diffraction effects are significant, diffracted intensities from different depths in the volume can interfere constructively or destructively as shown.

Two melt-spun Zr_xCu_{100-x} glasses were studied. The ribbons were jet-polished until perforation (Struers TenuPol 5, 33.3%:66.7% nitric acid:methanol, 233 K, 12 V, 100 mA), and then briefly ion-milled at low ion energies and temperature to remove the surface oxide (Gatan Precision Ion Polishing System, 5 min, 1 keV, 173 K, 2°). The specimens were kept under vacuum and examined within 48 h of preparation to limit oxide formation. This preparation regimen did not result in any de-vitrification (Liu *et al.*, 2013). An FEI Titan^3 80–300 FEGTEM (300 keV) with spherical (C_s) aberration correction of the imaging and probe-forming lenses was used to obtain SEND patterns of the glass (Fig. 1: aperture semi-angle α = 2.7 mrad, spherical aberration C_s = 0 mm, defocus Δf = 0 nm,

probe FWHM d_p = 0.51 nm). The spatial coherence function of this instrument has been measured under the relevant electron-optical conditions (Maunders *et al.*, 2011) and is, to an excellent approximation, perfectly coherent within the small angular range defined by the probe-forming aperture used here. This truncated spherical wavefield is imaged onto the specimen plane using a lens system with a lens aberration function given here to low order as a function of scattering vector, $|\mathbf{k}| = k = (k_x^2 + k_y^2)^{1/2}$ (Kirkland, 2010):

$$\chi(k) = -\pi\Delta f\lambda k^2 + \pi f a_2 \lambda k^2 \sin[2(\varphi - \varphi_{fa_2})] + 2\pi C_s \lambda^3 k^4 + 2\pi f a_3 \lambda^2 k^3 \sin[3(\varphi - \varphi_{fa_3})] + 2\pi f c_3 \lambda^2 k^3 \sin(\varphi - \varphi_{fc_3}).$$

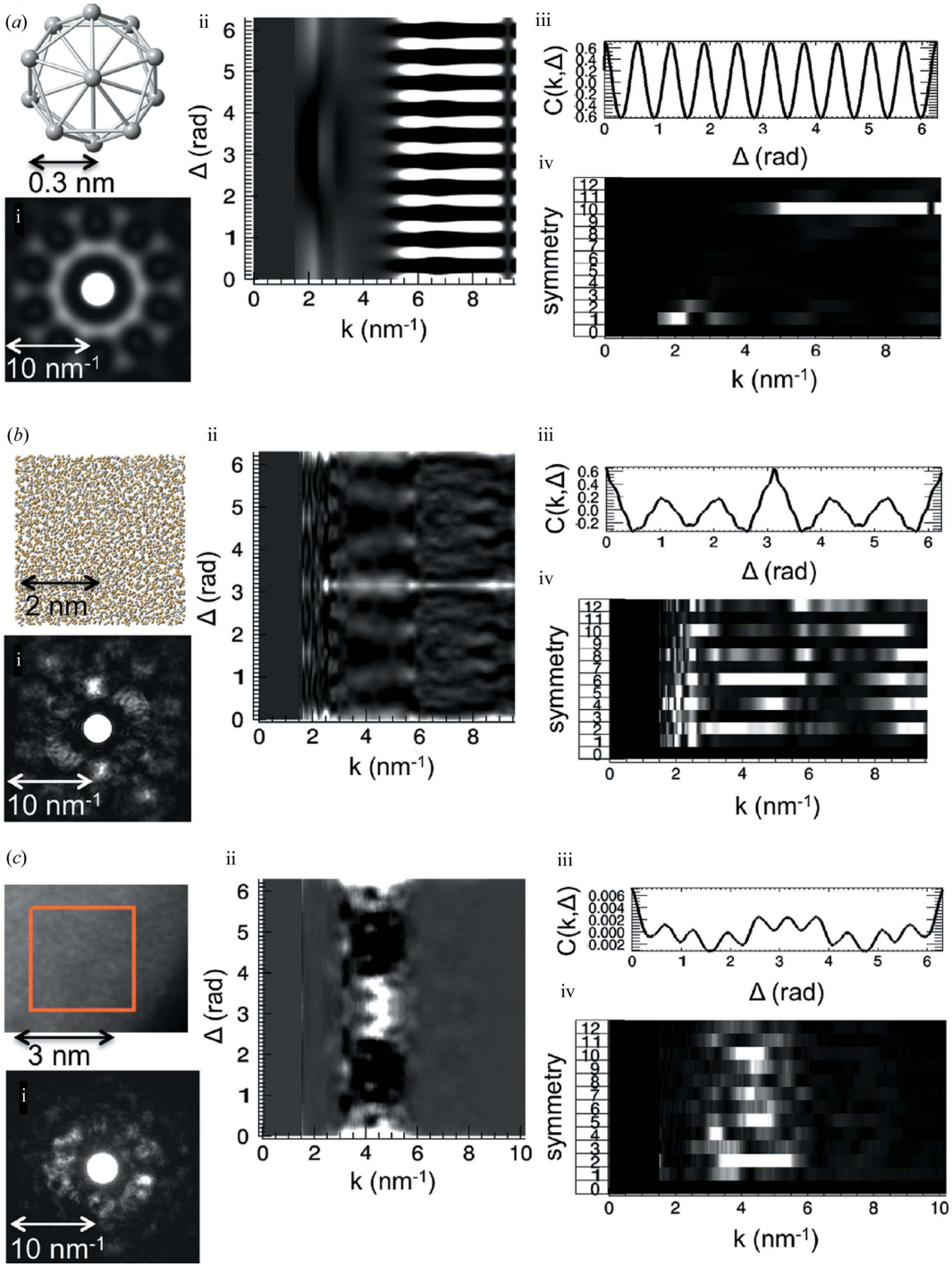

Figure 2
Simulated END patterns from a perfect icosahedron (*a*-i), a model (*b*-i) and experimental (*c*-i) $Zr_{36}Cu_{64}$ glass. Angular CCFs (*a*-ii), (*b*-ii), (*c*- ii), profiles of these CCFs from *k* within the first diffracted ring (*a*-iii), (*b*-iii), (*c*- iii), and magnitudes of the 0–12-fold symmetries in the CCFs (*a*-iv), (*b*-iv), (*c*-iv) from the icosahedron, model and experimental glass, respectively.

Here Δf is defocus, fa_2 is twofold astigmatism, fa_3 is threefold astigmatism, C_s is spherical aberration and fc_3 is coma. Defocus and spherical aberration are axially symmetric while the other aberrations included here vary with azimuthal angle.

The experimental convergence angle was selected for a given defocus and spherical aberration coefficient to bring the real-space resolution (probe size) down to the size of SRO clusters (~0.6 nm). A high-angle annular dark-field (HAADF) reference image was used to select regions for investigation (Fig. 2*c*). Arrays of 30 × 30 SEND patterns were collected from three 3.0 × 3.0 nm areas using a 1.5 s exposure time and a Gatan UltraScan CCD camera (2048 × 2048 binned to 512 × 512). Estimated thickness profiles were obtained using electron energy loss spectroscopy (EELS) and the log-ratio technique (Egerton, 1996). The thickness of the regions from which SEND patterns were obtained was ~5–10 nm (Liu *et al.*, 2013).

SEND patterns were simulated using IDL routines based on well known algorithms (Kirkland, 2010) using the kinematical, phase grating (Cowley & Moodie, 1959) and multislice approximations for the electron–specimen interaction (Cowley & Moodie, 1957). Perfect spatial coherence was assumed. The simulated structure was a 5000-atom model $Zr_{36}Cu_{64}$ (4 × 4 × 4 nm) obtained using molecular dynamics (MD) and embedded atom method (EAM) potentials (Mendelev *et al.*, 2009, 2010). The experimental (Fig. 2*c*-i) and simulated (phase grating, Fig. 2*b*-i) SEND patterns display diffracted intensities at the positions of the first and second diffraction rings for this glass [4.5 and 8.0 nm^{-1}, respectively (Mendelev *et al.*, 2010)] and a similar size of diffracted speckle to the un-diffracted disc, demonstrating that a similar low number of local clusters is being probed in each case. This number is 10–12 for the 4 nm-thick simulation cell.

To detect the subtle symmetries present in each SEND pattern recorded at probe position $\mathbf{r} = (x, y)$, we calculated the four-point angular cross-correlation function (CCF) defined by Wochner *et al.* (2009) as a function of scattering vector according to

$$C(\mathbf{r}, k, \Delta) = \frac{\langle I(k,\varphi)I(k,\varphi+\Delta)\rangle_\varphi - \langle I(k,\varphi)\rangle_\varphi^2}{\langle I(k,\varphi)\rangle_\varphi^2}. \qquad (1)$$

Here $I(k, \varphi)$ is the intensity diffracted into a given k and azimuthal angle, φ, and $\langle\rangle_\varphi$ denotes averaging over the azimuthal angle at a given k (Altarelli *et al.*, 2010). This function is related to the 'correlograph' (Gibson *et al.*, 2010) and correlation function (Howie *et al.*, 1985) that have been employed to uncover angular correlations in electron diffraction speckle patterns (Gibson *et al.*, 2010; Howie *et al.*, 1985).

Altarelli and co-workers have analysed the properties of the CCF assuming an orientationally disordered system of scatterers with prominent local structures (Altarelli *et al.*, 2010; Kurta *et al.*, 2012). They find that in the limit of either dilute systems or densely packed systems in which the illumination has a coherence length comparable to the size of the local cluster, as in this work, the CCF will demonstrate angular correlations reflecting symmetries of the local structural units (Altarelli *et al.*, 2010; Kurta *et al.*, 2012). Moreover, the magnitude of the symmetries present in the diffraction pattern can be accessed by decomposing the CCF at each k into a Fourier cosine series (Altarelli *et al.*, 2010) and obtaining the amplitude of each periodicity. Symmetries present/absent in the object may not be unambiguously present/absent in the diffraction pattern due to the projection geometry, dynamical diffraction, Ewald sphere curvature, an aberrated probe and other experimental constraints such as noise.

Fig. 2(*a*-i) displays the simulated END pattern from a single icosahedral cluster (Mendelev *et al.*, 2009, 2010) oriented down its fivefold axis. A perfect icosahedron has 30 twofold, 20 threefold and 12 fivefold symmetry axes, resulting in SEND patterns with distinct two-, six- and tenfold symmetries, respectively. Panels (*b*-i) and (*c*-i) of the same figure display simulated and experimental END patterns from a $Zr_{36}Cu_{64}$ glass. Simulations in this figure employ the phase grating approximation (Cowley & Moodie, 1959).

The corresponding CCFs from these patterns are displayed in Figs. 2(*a*-ii), 2(*b*-ii), 2(*c*-ii), respectively. Profiles through the CCFs from the first diffracted ring are shown in Figs. 2(*a*-iii), 2(*b*-iii), 2(*c*-iii). The SEND patterns from the experimental and model glasses have prominent tenfold and sixfold symmetries, respectively, not obvious prior to CCF analysis, while the SEND pattern from the icosahedral cluster shows strong tenfold symmetry. In general, the SEND patterns from glasses possess a number of different symmetries at various k that vary greatly from point to point. Strong symmetries in the experimental SEND patterns are mostly confined to the first diffracted ring, as the signal-to-noise ratio at higher scattering angles is low as we see in the CCF in Fig. 2(*c*-ii).

We plot the Fourier coefficient of each symmetry in the END patterns as a function of k and show this symmetry magnitude in Figs. 2(*a*-iv), 2(*b*-iv), 2(*c*-iv) for the 0–12-fold symmetries and for the icosahedral cluster and experimental and model glasses. The appearance of odd symmetries in the symmetry magnitude images from the experimental and model glasses (Figs. 2*b*-iv and 2*c*-iv) demonstrates the earlier noted breakdown of Friedel symmetry to varying degrees, with the experimental symmetry magnitude image showing more intense odd symmetries at higher k than simulation. Similar to X-ray microdiffraction simulation results (Altarelli *et al.*, 2010; Kurta *et al.*, 2012) the magnitude of symmetries in END patterns from local clusters in a metallic glass was optimized when the probe size was tuned to the size of the local cluster (Liu *et al.*, 2013). Specifically, the magnitude of the tenfold symmetry in an END from an on-axis icosahedron on top of 4 nm of glass was maximized when the probe size was equal to the cluster size. Qualitatively, a larger probe size sampled more clusters, reducing the magnitude of the tenfold symmetry, while a smaller probe and larger convergence angle resulted in overlapping diffracted intensities in the END, reducing the magnitude of the tenfold symmetry again (Liu *et al.*, 2013).

We may spatially average the symmetry magnitudes to investigate the nature of the predominant local structure. It

has been shown (Liu *et al.*, 2013) that these averaged symmetry magnitudes statistically sample the structure and also detect a number of strong symmetries associated with particular symmetric polyhedra (Fang *et al.*, 2010) that exist in the glass. We can also map individual symmetry magnitudes to examine the spatial extent of particular symmetries. Such symmetry maps will reflect the degree to which adjacent local structures share prominent symmetry axes in this glass. We average the magnitude of the two-, six- and tenfold symmetries over the width of the first diffraction ring ($3 \leq k \leq 6\ \mathrm{nm}^{-1}$) and map these averages. These maps are presented in Fig. 3 for the model glass with contrast ranges set to the maximum intensity in the tenfold symmetry maps. The averages of these maps reflect the symmetries in the SRO of the material.

In this work we concentrate on examining these average symmetry magnitudes from ensembles of 2700 patterns from experimental and simulated SEND patterns. We demonstrate that while the angular symmetries in an individual diffraction pattern may not be interpreted straightforwardly in terms of symmetries present in the object, there is an approach that will allow the average symmetry magnitudes to be interpreted in this way.

3. Results

3.1. Theoretical background

There can be a number of reasons for differences in the magnitude of opposing diffracted intensities in the S/TEM. The first we shall consider is Ewald sphere curvature, which can mean that nominally Friedel-related diffracted intensities are in fact arising from non-equivalent volumes in reciprocal space. The degree of Ewald sphere curvature can be calculated from geometry (Glaeser & Ceska, 1989):

$$z^* = \frac{1}{\lambda} - \left[\left(\frac{1}{\lambda}\right)^2 - \left(\frac{1}{d}\right)^2\right]^{1/2}. \qquad (2)$$

Here z^* is the magnitude of the curvature in reciprocal units (distance between the Ewald sphere at $1/d$ and the zero plane), λ is the wavelength and d is the real-space resolution. For 300 keV electrons, and examining symmetries in the first diffracted ring of a dense disordered material like a metallic glass, the magnitude of curvature is ten times smaller than the reciprocal thickness of the specimen and thus Ewald sphere curvature is not expected to contribute greatly to the breakdown of Friedel's law.

Even if the weak-phase or kinematical approximation could be applied to the electron beam interaction with the specimen, an imaginary component in the original probe wavefunction arising from lens aberrations can give rise to asymmetry in diffraction patterns made using a converged probe (Rodenburg, 1988; Hÿtch & Chevalier, 1995). Following previous work (Hÿtch & Chevalier, 1995), we write for the specimen exit wave

$$\psi(\mathbf{r}) = \psi_0(\mathbf{r}) \exp[i\sigma v(\mathbf{r})]. \qquad (3)$$

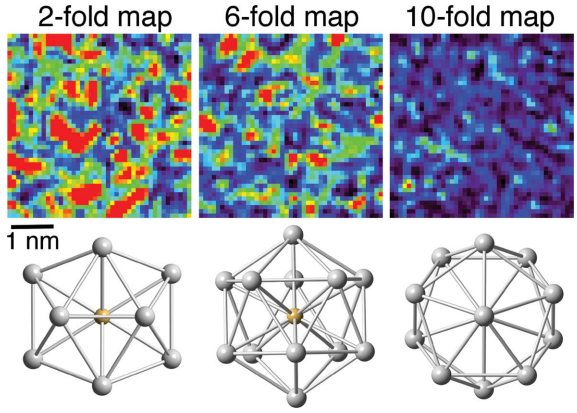

Figure 3
Two-, six- and tenfold symmetry maps produced from simulated SEND patterns from the model $Zr_{36}Cu_{64}$ glass. Contrast for the simulated and experimental maps has been scaled to the maximum intensity in the tenfold map.

Here $\psi_0(\mathbf{r})$ is the probe wavefunction and $v(\mathbf{r})$ is the projected potential according to

$$v(\mathbf{r}) = \int v(x, y, z)\, \mathrm{d}z. \qquad (4)$$

In the weak-phase object limit we can approximate this as

$$\psi(\mathbf{r}) = \psi_0(\mathbf{r}) + i\sigma\psi_0(\mathbf{r})v(\mathbf{r}). \qquad (5)$$

The disturbance in the back focal plane is then

$$\Psi(\mathbf{k}) = \Psi_0(\mathbf{k}) + i\sigma\Psi_0(\mathbf{k}) * V(\mathbf{k}). \qquad (6)$$

Here $\Psi(\mathbf{k}) = \mathcal{F}[\psi(\mathbf{r})]$, $\Psi_0(\mathbf{k}) = \mathcal{F}[\psi_0(\mathbf{r})]$, $V(\mathbf{k}) = \mathcal{F}[v(\mathbf{r})]$, where $\mathcal{F}[]$ denotes a Fourier transform.

Putting $\Psi_d(\mathbf{k}) = i\sigma\Psi_0(\mathbf{k}) * V(\mathbf{k})$ we can write for the diffracted intensity

$$\begin{aligned} I(\mathbf{k}) &= |\Psi(\mathbf{k})|^2 \\ &= |\Psi_0(\mathbf{k}) + \Psi_d(\mathbf{k})|^2 \\ &= |\Psi_0(\mathbf{k})|^2 + |\Psi_d(\mathbf{k})|^2 + 2\mathrm{Re}\left[\Psi_0^*(\mathbf{k})\Psi_d(\mathbf{k})\right]. \end{aligned} \qquad (7)$$

If any of the three terms in this equation are not symmetric with the substitution $\mathbf{k} \rightarrow -\mathbf{k}$ then Friedel's law will be broken. The first term will be symmetric with such a substitution if the probe is a real function, that is, there is no significant phase variation across the objective aperture from aberrations. The second term will also be symmetric if the probe and object functions are real. To see this explicitly we write

$$\begin{aligned} \Psi_d^*(-\mathbf{k}) &= -i\sigma\Psi_0^*(-\mathbf{k}) * V^*(-\mathbf{k}) \\ &= -i\sigma\Psi_0(\mathbf{k}) * V(\mathbf{k}) \\ &= -\Psi_d(\mathbf{k}). \end{aligned} \qquad (8)$$

Lens aberrations will introduce an imaginary component to this diffracted wavefunction, and the symmetry will be broken. Finally, the third term that represents interference between the undiffracted and diffracted wavefunctions will also be asymmetric, for a non-centrosymmetric object and for the values of k where the two beams are of similar magnitude. Thus, as noted by Rodenburg (1988) and Hÿtch & Chevalier

(1995), lens aberrations can introduce significant asymmetry in END patterns of general disordered objects even if the kinematical approximation holds.

Considering a general object with no centre of symmetry, if dynamical effects are taken into account, and even if the incident probe has no aberrations, Friedel's law will be broken (Cowley & Moodie, 1959). Assuming a real probe wavefunction of unit magnitude, in the phase grating approximation (Cowley & Moodie, 1959), we can write for the specimen exit wave

$$\psi(\mathbf{r}) = \exp[i\sigma v(\mathbf{r})]. \tag{9}$$

The wavefunction in the back focal plane is thus

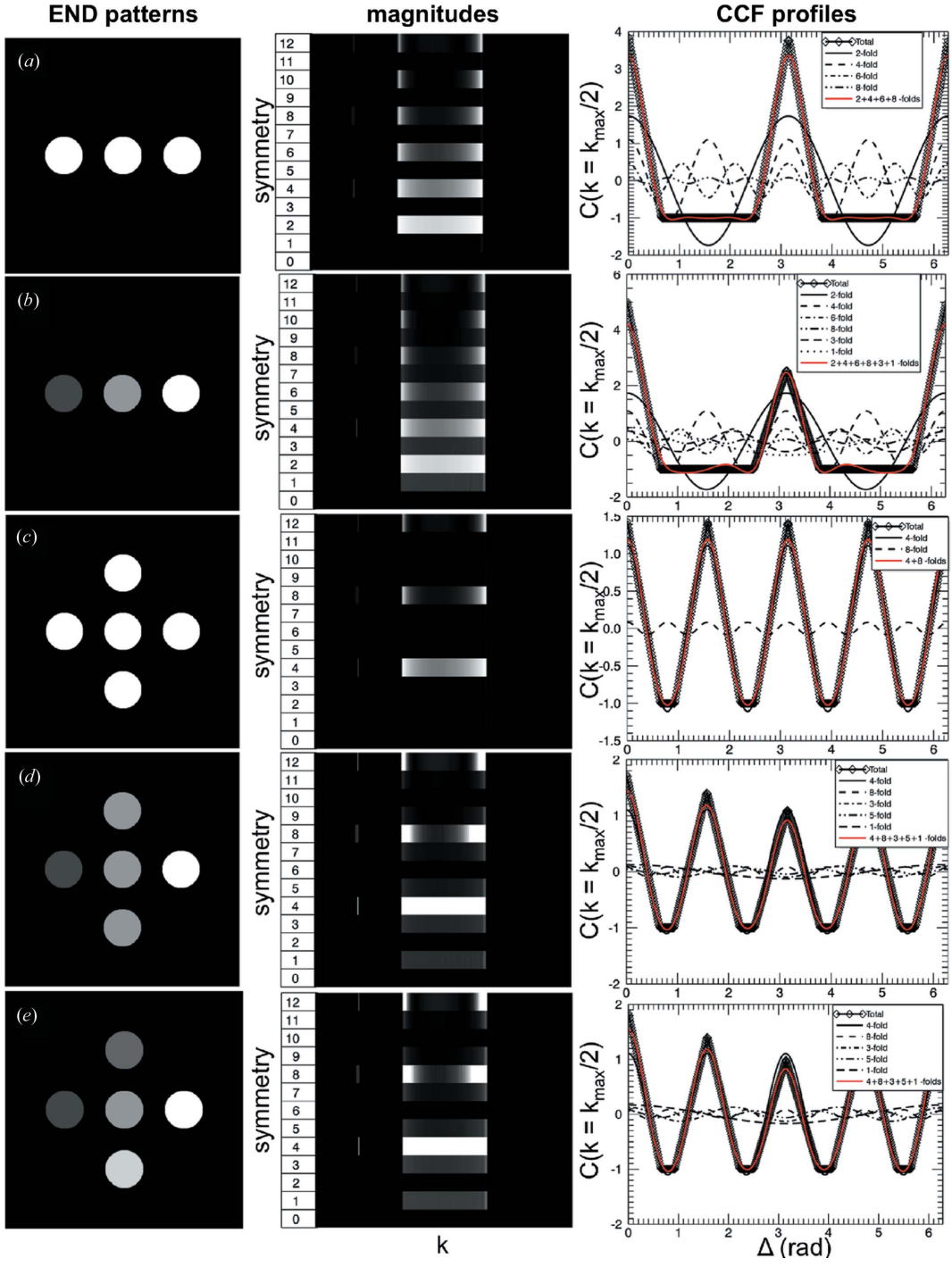

Figure 4
Ideal END patterns, corresponding symmetry magnitudes and profiles through the CCF with main Fourier components overlaid for twofold symmetry in the kinematical (*a*) and dynamical (*b*) cases, and fourfold symmetry in the kinematical (*c*), dynamical (involving one Friedel pair) (*d*) and dynamical (involving both Friedel pairs) (*e*) cases.

$$\Psi(\mathbf{k}) = \mathcal{F}\{\exp[i\sigma v(\mathbf{r})]\} = \mathcal{F}\{\cos[\sigma v(\mathbf{r})]\} + i\mathcal{F}\{\sin[\sigma v(\mathbf{r})]\}. \quad (10)$$

For a general object we can write (Cowley & Moodie, 1959)

$$\Psi(\mathbf{k}) = \delta(\mathbf{k}) + i\sigma S(\mathbf{k}) - \frac{\sigma^2}{2}[S(\mathbf{k}) * S(\mathbf{k})] + \ldots \quad (11)$$

We define the kinematic structure factor $S(\mathbf{k})$ or single scattering distribution:

$$S(\mathbf{k}) = \sum_j f_j(\mathbf{k}) \exp(2\pi i \mathbf{k}\cdot\mathbf{r}). \quad (12)$$

The sum is undertaken over all the atoms j in the diffracting column with atomic scattering factors $f_j(\mathbf{k})$. This single scattering distribution is analogous to the kinematical structure factor for a crystal (Cowley & Moodie, 1959) but is a continuous distribution in reciprocal space, rather than existing only at reciprocal-lattice points.

$\Psi(\mathbf{k})$ is the sum of the Fourier transform of a cos and sin term, both of which are complex for structures lacking a centre of symmetry. Following a line of argument developed by Cowley, we write the cos term as the sum of symmetric and anti-symmetric components:

$$\cos[\sigma v(\mathbf{r})] = \tfrac{1}{2}\{\cos[\sigma v(\mathbf{r})] + \cos[\sigma v(-\mathbf{r})]\} + \tfrac{1}{2}\{\cos[\sigma v(\mathbf{r})] - \cos[\sigma v(-\mathbf{r})]\}. \quad (13)$$

We denote Fourier transforms of these components as $C_{\cos}$ and $iA_{\cos}$. The sin component can be treated in the same way. Thus

$$\Psi(\mathbf{k}) = C_{\cos} + iA_{\cos} + i(C_{\sin} + iA_{\sin}) = C_{\cos} - A_{\sin} + i(C_{\sin} + A_{\cos}) \quad (14)$$

$$I(\mathbf{k}) = |\Psi(\mathbf{k})|^2 = (C_{\cos} - A_{\sin})^2 + (C_{\sin} + A_{\cos})^2 \quad (15)$$

$$I(-\mathbf{k}) = (C_{\cos} + A_{\sin})^2 + (C_{\sin} - A_{\cos})^2. \quad (16)$$

For a centrosymmetric crystal the anti-symmetric components equal zero and thus $I(\mathbf{k}) = I(-\mathbf{k})$. If the structure has no centre of symmetry, as for the disordered structures we investigate here, then in general

$$I(\mathbf{k}) = I_1 + I_2 \quad (17)$$

$$I(-\mathbf{k}) = I_1 - I_2. \quad (18)$$

Here we define $I_1 = C_{\cos}^2 + A_{\sin}^2 + C_{\sin}^2 + A_{\cos}^2$ and $I_2 = -2C_{\cos}A_{\sin} + 2C_{\sin}A_{\cos}$.

This symmetry degradation due to dynamical diffraction also holds in the more general case of dynamical scattering in the multislice and scattering matrix formalisms (Cowley & Moodie, 1959; Fujimoto, 1959). For non-centrosymmetric structures the intensities of opposing Friedel pairs have a similar form to the phase grating case, but include higher-order terms:

$$I(\mathbf{k}) = |\Psi(\mathbf{k})|^2 = I_a + I_b + \ldots \quad (19)$$

$$I(-\mathbf{k}) = |\Psi(-\mathbf{k})|^2 = I_a - I_b + \ldots \quad (20)$$

The I_a coincide with the kinematical result, and represent scattering up to the second power of crystal thickness in the scattering matrix expansion (Fujimoto, 1959). The I_b are the terms up to the third power in crystal thickness. These terms and other higher-order odd terms in the expansion vanish for centrosymmetric crystals, and cause a breakdown in Friedel symmetry for non-centrosymmetric structures. The scattering matrix expansion in thickness coincides with the multislice approach of Cowley & Moodie (Fujimoto, 1959).

Dynamical scattering thus reduces the magnitude of a twofold symmetry in an END pattern and increases the contribution into a onefold symmetry. Consider a single pair of angularly opposing diffracted intensities $I(k, \varphi_1) = I(k, \varphi_1 + \pi)$ in the kinematical case. This will result in a non-zero contribution to the CCF at $(k, \Delta = 0)$ and $(k, \Delta = \pi)$ that we write as

$$C(k, \Delta = 0) = C(k, \Delta = \pi) = I(k, \varphi_1)I(k, \varphi_1 + \pi) + I(k, \varphi_1)I(k, \varphi_1 + \pi) = 2I(k, \varphi_1)^2. \quad (21)$$

We omit terms at other values of azimuthal angle, φ, and the normalizing factor equal to the intensity averaged over φ. In the case that includes dynamical scattering the contributions to the CCF at $\Delta = 0$ and $\Delta = \pi$ are not equal:

$$C(k, \Delta = 0) = (I_1 + I_2)^2 + (I_1 - I_2)^2 = 2I_1^2 + 2I_2^2 \quad (22)$$

$$C(k, \Delta = \pi) = (I_1 + I_2)(I_1 - I_2) + (I_1 + I_2)(I_1 - I_2) = 2I_1^2 - 2I_2^2. \quad (23)$$

Thus the magnitude of the twofold symmetry is reduced and instead there is a contribution to a onefold symmetry.

This effect is shown explicitly in Fig. 4. This figure displays ideal END discs with twofold symmetry in the kinematical case [(*a*) $I_2 = 0$] and the dynamical case [(*b*) $I_2 \neq 0$]. The symmetry magnitudes from the Fourier decomposition and a profile through the CCF with the largest terms in the decomposition overlaid are shown to the right of the END patterns. From these panels it is clear that in the kinematical case, only even symmetries are observed, as expected. In this case higher-order even symmetries occur to fit the flat regions in the CCF, an effect which will be minimal with background intensity. Dynamical effects manifest as a decrease in the even symmetry magnitudes and an increase in the odd symmetries with the greatest magnitude increase in the odd symmetry just below the pattern's dominant even symmetry. A similar effect is seen for the fourfold case [(*c*) kinematical, (*d*) dynamical with asymmetric intensities of one Friedel pair, (*e*) dynamical with asymmetric intensities of both Friedel pairs with $I_3 \neq I_2$]. Again, dynamical diffraction results in a 'leakage' of symmetry magnitude in the diffraction pattern into the odd symmetry one channel below the dominant even symmetry. The reason for this can be seen from the breakdown into Fourier components. The odd symmetries are required to reduce the magnitudes of the dominant even symmetry. Dynamical

diffraction of all reflections (panel *e*) increases this effect. The effect is also observed for all higher symmetries in an END pattern, *i.e.* sixfold and tenfold.

Finally, we expect that experimental instabilities such as noise in the charge-coupled device (CCD) camera may also contribute to the non-equivalence of Friedel-related diffraction pairs. We examine the effect of lens aberrations, dynamical diffraction and camera noise on angular symmetry in END by simulation.

3.2. Analysis of SEND patterns

Figs. 5(*a*), 5(*b*) and 5(*c*) show simulated END patterns from the same volume in the model glass employing the kinematical, phase object and multislice approximations, respectively. In panel (*d*) we show a simulated END pattern employing the phase object approximation with a large twofold astigmatism (500 nm). By inspection, it is difficult to see any differences between the diffraction patterns. However, when the magnitudes of symmetries in the END patterns are compared quantitatively there are clear differences, with odd symmetries appearing in the phase grating, multislice and aberrated examples. We statistically analysed the symmetries present in the END pattern employing various electron diffraction approximations (kinematical, phase grating, multislice) and including noise and large values of aberration coefficient. To do this, we averaged the symmetry magnitudes in the first diffracted ring ($3 \leq k \leq 6$ nm^{-1}) from an ensemble of 900 simulated nanodiffraction patterns. Such an averaging technique has been found to be critical to obtaining a stable estimate of the degree of Friedel symmetry in END patterns from amorphous materials (Sun *et al.*, 2014). We averaged results from the atomic model in three orthogonal orientations and cite the standard deviation in these measurements as the error.

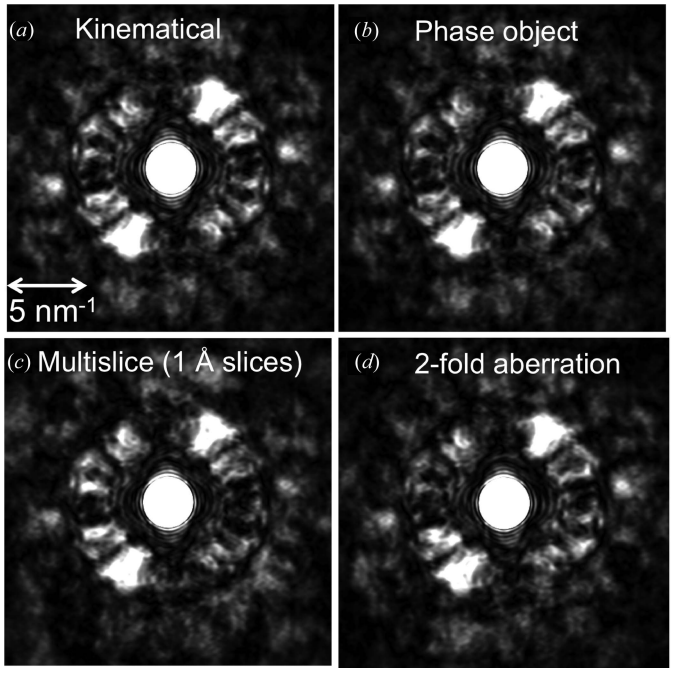

Figure 5
Simulated END patterns from the same volume of a model $Zr_{36}Cu_{64}$ glass (aperture semi-angle α = 2.7 mrad, spherical aberration C_s = 0 mm, defocus Δf = 0 nm, probe FWHM d_p = 0.51 nm) employing the following approximations: (*a*) kinematical, (*b*) phase object, (*c*) multislice (1 Å slices) and (*d*) phase object with large twofold astigmatism (fa_2 = 500 nm).

Fig. 6 shows plots of the averaged symmetry magnitudes for the following scenarios. Fig. 6(*a*) shows symmetry magnitudes from END patterns with 0.3%, 1%, 3%, 10% and 20% noise corresponding to average counts of 100 000, 10 000, 1000, 100 and 25. To simulate the presence of noise a random Poisson deviate was added to simulated END patterns that were multiplied by the average number of counts. The average experimental noise level was 3% corresponding to average diffracted counts of 1000. Fig. 6(*b*) shows the symmetry magnitudes in the phase object approximation with no aberrations, typical measured aberrations for the experimental conditions (Δf = −1.13 nm, fa_2 = 4.609 nm, fa_3 = 20.66 nm, fc_3 = 6.099 nm, C_s = −280 nm), and large values of spherical aberration (C_s = 10 000 nm), twofold astigmatism (fa_2 = 500 nm) and coma (fc_3 = 200 nm). The aberrated probes are shown in Fig. 7. Figs. 6(*c*) and 6(*d*) show the average symmetry magnitudes for 40 Å-thick and 80 Å-thick models calculated

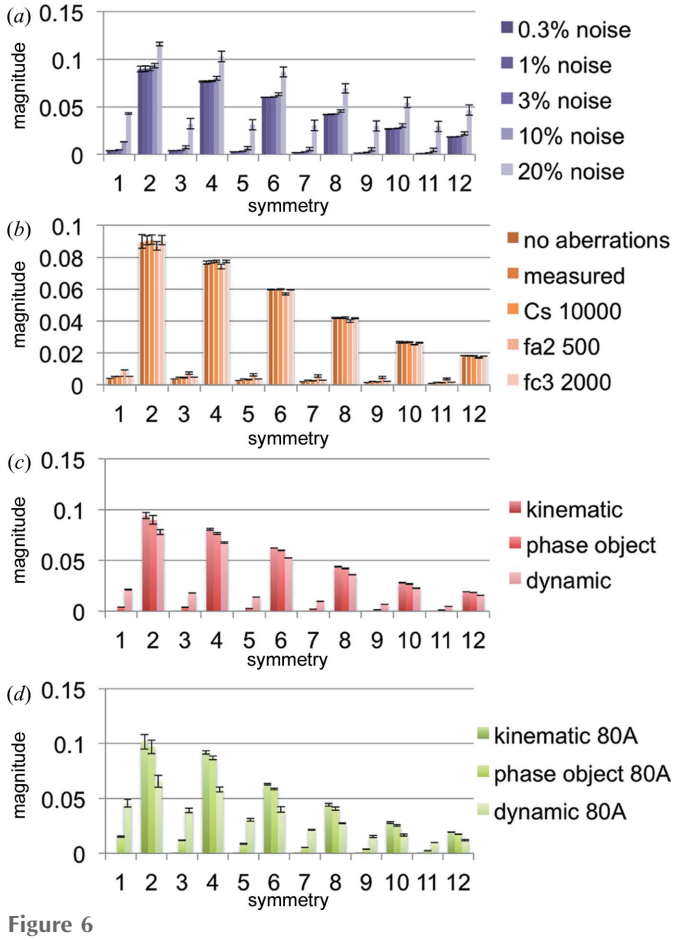

Figure 6
Average symmetry magnitudes in the presence of (*a*) noise, (*b*) lens aberrations, and employing different diffraction approximations for a (*c*) 40 Å- and (*d*) 80 Å-thick model.

in the kinematical, phase grating and multislice (1 Å-thick slices) approximations. The 80 Å models were constructed by rotating and stacking the 40 Å-thick models.

From examining Fig. 6(*a*), it is clear that noise at experimental levels does not appreciably change the average symmetry magnitudes. Interestingly, noise at higher levels (10% and 20%) increases both the odd and even symmetry magnitudes. Fig. 6(*b*) shows that using a small convergence angle of 2.3 mrad and an aberration corrector to correct the probe-forming lens means that lens aberrations of the measured magnitude do not significantly alter the symmetry magnitudes. Also, axially symmetric aberrations such as C_s do not change the symmetry magnitudes even when they are present at high levels. Non-axial aberrations such as twofold astigmatism do increase the degree of odd symmetry magnitudes at the expense of even symmetries. However, coma, which is also non-axial, does not seem to have the same effect, since it does not result in a non-symmetric probe. Figs. 6(*c*) and 6(*d*) show that including dynamical effects does increase the magnitudes of odd symmetries and decrease the magnitudes of the even symmetries. In the case of the phase grating approximation, which takes into account changes in electron phase based on atom position, but still retains the projection approximation, there are small additional contributions to the odd symmetries. Modelling dynamical effects more exactly using a multislice calculation increases the magnitude of odd symmetries. Comparing Figs. 6(*c*) and 6(*d*) we see that doubling the thickness of the glass results in a twofold increase in odd symmetry magnitudes for the multislice simulations, and a more than twofold increase in the phase grating approximation.

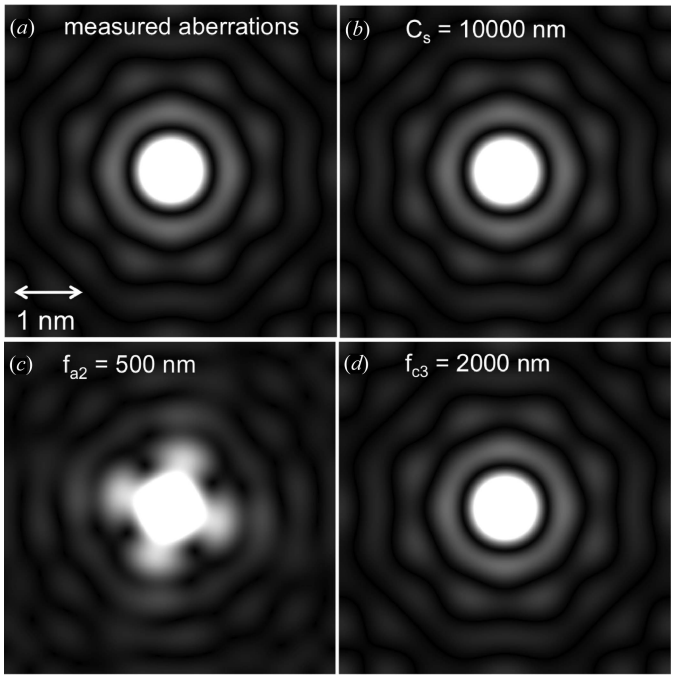

Figure 7
Aberrated probes used to simulate END patterns contributing to averaged symmetry magnitudes presented in Fig. 6(*b*).

For an amorphous material with symmetric SRO units such as a close-packed metallic glass, one can then interpret the following scenario for diffraction. Projection of the structure onto a plane reduces the symmetry of the diffraction pattern compared to the symmetry of the original object. Dynamical diffraction between SRO clusters at different heights reduces the symmetry in the diffraction pattern further as diffracted intensities become distributed between multiple sets of 'reflections'. This re-distribution of diffraction intensity in a single END pattern is challenging to interpret in the absence of an exact atomic model. However, we will demonstrate that statistical information of symmetries in an ensemble of END patterns can give insight into average symmetries present in the structure.

Fig. 8(*a*) shows the average symmetry magnitudes in SEND from two experimental melt-spun Zr_xCu_{100-x} glasses and below this in (*b*) and (*c*) the simulated symmetry magnitudes from the 40 Å- and 80 Å-thick models. The thickness of the experimental glasses was estimated using EELS as being between 5 and 10 nm. From comparison with the degree of odd symmetries and thus asymmetry in the Friedel diffraction pairs in the models, we see that the experimental thickness is most likely to be closer to 8 nm. As shown above in the analysis based on the phase grating and dynamical diffraction formalisms, dynamical effects result in Friedel-pair asymmetry

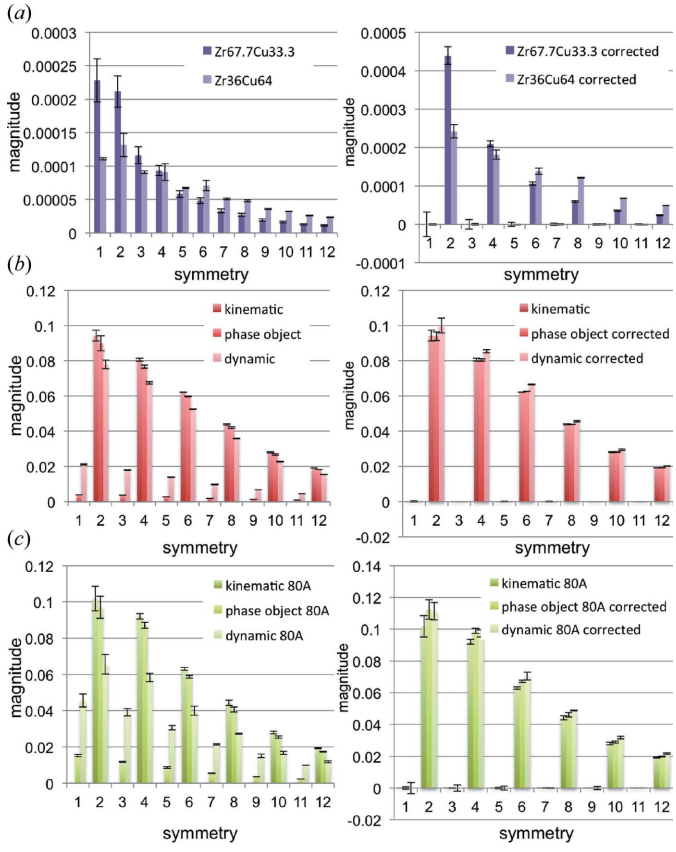

Figure 8
Average symmetry magnitudes from experimental glass (*a*) and the (*b*) 40 Å- and (*c*) 80 Å-thick model. On the left are the uncorrected symmetry magnitudes. On the right are the symmetry magnitudes corrected to regain the single scattering symmetry magnitudes.

according to the simple rule of one spot having a deficit intensity while the opposing spot has an equal amount of surplus intensity. This means that dynamical scattering will cause even symmetries to 'leak' into odd symmetries one channel down. As a first approximate correction to regaining the kinematical symmetry in these averaged magnitudes, we suggest adding the magnitude in the odd symmetries into the even symmetry one channel up. We correct the symmetry magnitudes on the left of Fig. 8 according to this procedure and dislay these corrected magnitudes on the right of Fig. 8. As seen in these corrected symmetry magnitudes from the simulations, this procedure does result in corrected dynamical symmetry magnitudes that compare quantitatively with the kinematical ones. The same procedure results in symmetry magnitudes for the experimental glasses that are significantly different. We suggest that these corrected symmetry magnitudes now reflect symmetries of the projected structure without the need to interpret diffracted intensities in individual END. In materials with a limited number of high-symmetry structural units in the diffracting volume the corrected symmetries may now be interpreted more directly to understand changes to the SRO of the materials with composition or preparation history. While the average kinematical symmetries may be perhaps more readily interpreted as reflecting actual symmetries in the object, these only recover the magnitude squared of the Fourier transform of the projected object, and structural information is lost. It is clear that the subsequent odd symmetries that appear in the END patterns due to dynamical diffraction contain valuable additional information about the three-dimensional structure of the object.

4. Conclusion

Angular symmetries in electron nanodiffraction patterns are examined in the context of lens aberrations, camera noise and dynamical diffraction effects. Simulations demonstrated that dynamical diffraction was chiefly responsible for odd symmetries in electron nanodiffraction patterns under conditions in modern aberration-corrected microscopes. The difference in the intensity of nominally Friedel-related diffraction pairs for disordered structures was found to have a simple form. This allowed an approximate correction to be applied to average dynamical diffraction pattern angular symmetry magnitudes which recovered the kinematical symmetry magnitudes. These can be interpreted in terms of the symmetry of the actual projected object. In the case of the simulated data for model thicknesses of 4–8 nm this correction was accurate within numerical uncertainty.

Acknowledgements

ACYL gratefully acknowledges the support of the Science Faculty and the Monash Centre for Electron Microscopy (MCEM), Monash University. The electron microscopy was performed in the MCEM. We thank Mr Renji Pan, Dr Russell King and Dr Matthew Weyland of the MCEM for their assistance. The FEI Titan^3 80–300 FEGTEM was funded by the Australian Research Council (LE0454166). Samples were prepared and MD simulations were performed at Ames Laboratory, funded by OS, BES under contract No. DE-AC02-07CH11358. We thank Dr M. Besser and Dr M. Mendelev for their contributions.

References

Altarelli, M., Kurta, R. P. & Vartanyants, I. A. (2010). *Phys. Rev. B*, **82**, 104207.
Cowley, J. M. (2002). *Ultramicroscopy*, **90**, 197–206.
Cowley, J. M., Buseck, P. & Eyring, L. (1988). *Imaging Theory*, p. 46. New York: Oxford University Press.
Cowley, J. M. & Moodie, A. F. (1957). *Acta Cryst.* **10**, 609–619.
Cowley, J. M. & Moodie, A. F. (1959). *Acta Cryst.* **12**, 360–367.
Egerton, R. F. (1996). *Electron Energy-Loss Spectroscopy in the Electron Microscope*, 2nd ed. New York: Plenum.
Fang, X. W., Wang, C. Z., Yao, Y. X., Ding, Z. J. & Ho, K. M. (2010). *Phys. Rev. B*, **82**, 184204.
Fujimoto, F. (1959). *J. Phys. Soc. Jpn*, **14**, 1558–1568.
Gibson, J. M., Treacy, M. M. J., Sun, T. & Zaluzec, N. J. (2010). *Phys. Rev. Lett.* **105**, 125504.
Glaeser, R. M. & Ceska, T. A. (1989). *Acta Cryst.* A**45**, 620–628.
Howie, A., McGill, C. A. & Rodenburg, J. M. (1985). *J. Phys. Colloq.* **46-C9**, 59–62.
Hÿtch, M. J. & Chevalier, J. P. (1995). *Ultramicroscopy*, **58**, 114–121.
Kirkland, E. J. (2010). *Advanced Computing in Electron Microscopy*, 2nd ed. Berlin, Heidelberg, New York: Springer.
Kurta, R. P., Altarelli, M., Weckert, E. & Vartanyants, I. A. (2012). *Phys. Rev. B*, **85**, 184204.
Liu, A. C. Y., Neish, M. J., Stokol, G., Buckley, G. A., Smillie, L. A., de Jonge, M. D., Ott, R. T., Kramer, M. J. & Bourgeois, L. (2013). *Phys. Rev. Lett.* **110**, 205505.
Maunders, C., Dwyer, C., Tiemeijer, P. & Etheridge, J. (2011). *Ultramicroscopy*, **111**, 1437–1446.
Mendelev, M. I., Kramer, M. J., Ott, R. T., Sordelet, D. J., Besser, M. F., Kreyssig, A., Goldman, A. I., Wessels, V., Sahu, K. K., Kelton, K. F., Hyers, R. W., Canepari, S. & Rogers, J. R. (2010). *Philos. Mag.* **90**, 3795–3815.
Mendelev, M. I., Kramer, M. J., Ott, R. T., Sordelet, D. J., Yagodin, D. & Popel, P. (2009). *Philos. Mag.* **89**, 967–987.
Rodenburg, J. M. (1988). *Ultramicroscopy*, **25**, 329–343.
Sun, T., Treacy, M. M. J., Li, T., Zaluzec, N. J. & Gibson, J. M. (2014). *Microsc. Microanal.* **20**, 627–634.
Treacy, M. M. J. & Borisenko, K. B. (2012). *Science*, **335**, 950–953.
Treacy, M. M. J., Gibson, J. M., Fan, L., Paterson, D. J. & McNulty, I. (2005). *Rep. Prog. Phys.* **68**, 2899.
Wochner, P., Gutt, C., Autenrieth, T., Demmer, T., Bugaev, V., Ortiz, A. D., Duri, A., Zontone, F., Grübel, G. & Dosch, H. (2009). *Proc. Natl Acad. Sci. USA*, **106**, 11511–11514.
Ziman, J. M. (1979). *Models of Disorder: the Theoretical Physics of Homogeneously Disordered Systems.* Cambridge University Press.
Zuo, J.-M. & Tao, J. (2011). *Scanning Electron Nanodiffraction and Diffraction Imaging*, p. 393. New York, Dordrecht, Heidelberg, London: Springer.